Operando tracking of ion population changes in the EDL electrode of a lithium-ion capacitor during its charge/discharge

Andres Parejo-Tovar, Céline Merlet, Paula Ratajczak, François Béguin

Energy Storage Materials 73 (2024) 103810

Contents lists available at ScienceDirect

Energy Storage Materials

journal homepage: www.elsevier.com/locate/ensm

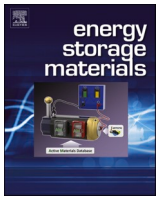

Operando tracking of ion population changes in the EDL electrode of a lithium-ion capacitor during its charge/discharge

Andres Parejo-Tovar [a], Céline Merlet [b], Paula Ratajczak [a], François Béguin [a,*]

[a] *Institute of Chemistry and Technical Electrochemistry, Poznan University of Technology, Berdychowo 4, 60-965 Poznan, Poland*
[b] *CIRIMAT, Université Toulouse 3 Paul Sabatier, Toulouse INP, CNRS, Université de Toulouse, 118 Route de Narbonne, 31062, Toulouse cedex 9, France*

ARTICLE INFO

Keywords:
Lithium-Ion Capacitor
EDL electrode
Operando electrochemical dilatometry
In situ potentiostatic electrochemical impedance spectroscopy
Operando Raman spectroscopy
Ion population changes
Ion trapping

ABSTRACT

This study elucidates in-pore ion population changes in an activated carbon (AC)-based electrode operating within an extended potential range, akin to the positive electrode of a lithium-ion capacitor (LIC). Molecular dynamics (MD) simulations applied to a battery-type electrolyte (1 mol L^{-1} $LiPF_6$ in EC:DMC), both in bulk and adsorbed within a model porous carbon, reveal partial solvation of Li^+ cations within the pores and complete desolvation of PF_6^- anions in both states. *Operando* electrochemical dilatometry (ECD), *in situ* potentiostatic electrochemical impedance spectroscopy, and *operando* Raman spectroscopy on AC electrodes confirm: (i) ionic exchange followed by anion adsorption during initial hole injection from the point of zero charge (*PZC*) to 4.5 V *vs.* Li/Li^+; (ii) desorption and peak liberation of trapped PF_6^- at 3.2 V *vs.* Li/Li^+ during hole withdrawal; (iii) permselective adsorption of partially solvated Li^+ during electron injection down to 2.2 V *vs.* Li/Li^+; (iv) cation desorption during electron withdrawal up to *PZC* followed by similar ionic exchange and anion adsorption (as described in (i)) at potentials above the *PZC*, however with peak liberation of trapped Li^+ at 3.8 V *vs.* Li/Li^+. The high polarization required to extract trapped ions from the pores may explain the reduced lifespan of LICs, requiring further work to eliminate trapping by optimizing porous texture.

1. Introduction

Electrical double-layer capacitors (EDLCs) are widely recognized as high-power energy storage devices due to the physical nature of their charge/discharge mechanism, which relies on the reversible electrostatic accumulation of ions at the electrode-electrolyte interface. EDLCs typically feature electrodes made from nanoporous carbon with a high surface area, often activated carbon (AC). AC is favored for its excellent electrical conductivity, robust chemical and thermal stability, diverse morphologies, and tunable porous texture [1]. The performance of EDLCs is significantly influenced by the choice of the electrolyte, which ideally should exhibit high ionic conductivity to enhance the specific power and a wide electrochemical stability window (*ESW*) to improve energy storage/release and extend the device's lifespan [2,3]. Consequently, most commercially available EDLCs use electrolytes based on organic solvents, with 1 mol L^{-1} tetraethylammonium tetrafluoroborate ($TEABF_4$) in acetonitrile being a common choice due to its relatively high ionic conductivity and low viscosity [4]. These formulations allow the devices to achieve rated voltage values as high as 2.85–3.0 V [5]. Despite their interesting features, EDLCs have some limitations, such as low specific energy values, typically in the range of 6–8 Wh kg^{-1} [6], and a high rate of self-discharge compared to other energy storage systems (ESSs) [7]. These drawbacks may hinder their use as a primary power source in hybrid vehicles and limit their integration into electrical power grids. Given the growing interest in transport electrification and the rapid development of high-power delivery applications, researchers are actively seeking long-lasting ESSs that can store and deliver more energy than EDLCs while maintaining high power output.

In this context, metal-ion capacitors (MICs) combining an electrical double-layer (EDL) positive electrode and a battery-type negative electrode have emerged as a promising energy storage technology [8] due to two notable features: (i) the negative electrode operates at low potential, thus, the maximum operative voltage of MICs is significantly higher than that of an AC//AC capacitor, generally reaching up to 3.8 V; (ii) the EDL-positive electrode operates in a wider potential range than the positive electrode of an EDLC, typically between 2.5 V and 4.1 V *vs.* Na/Na^+ for a sodium-ion capacitor [8], resulting in a capacity/capacitance of the device that is larger than in a conventional EDLC [8,9]. This unique configuration enables MICs to achieve up to approximately four times higher specific energy than EDLCs at comparable power levels [6,

* Corresponding author.
E-mail address: francois.beguin@put.poznan.pl (F. Béguin).

https://doi.org/10.1016/j.ensm.2024.103810
Received 16 July 2024; Received in revised form 14 September 2024; Accepted 23 September 2024
Available online 28 September 2024

10,11]. In addition, the presence of the battery-type negative electrode contributes to a self-discharge rate of less than 5% after three months at 25 °C [10], which is a significant advantage over EDLCs. The most representative example of MICs is the lithium-ion capacitor (LIC), which has been reported in the literature to achieve between 10,000 and 100,000 charge/discharge cycles [6,12]. The lower life span of MICs compared to EDLCs may be due to faster ageing of the positive EDL electrode during cycling.

Owing to the distinctive features of MICs, the operative mechanism of the EDL positive electrode in this type of hybrid capacitor has become a captivating subject for study, given its operation in an extended range of potential. Fig. 1 schematically represents the potential variations of electrodes and hypothesized charge exchange processes during a complete galvanostatic cycle of a LIC in $LiPF_6$-based electrolyte (after the pre-lithiation of the negative electrode) described in reference [13]. This cycle can be divided into three steps: *i)* during the first charge of the LIC, the positive AC electrode is polarized at a potential higher than the point of zero charge (*PZC*) up to its oxidation potential limit (E_{max}), while PF_6^- anions from the electrolyte are electrosorbed in the porosity; *ii)* during the discharge, the PF_6^- anions are desorbed until the electrode reaches *PZC*, after which lithium cations from the electrolyte are electrosorbed in the AC electrode until the reduction potential limit of the electrolyte (E_{min}); *iii)* finally, as the AC electrode is polarized up to *PZC* during the subsequent charging of the LIC, lithium cations are desorbed back into the electrolyte. Although the sequence proposed in reference [13] seems logical, there is no experimental evidence to support it; therefore, further investigation is required to understand the charge exchange processes occurring in the positive AC electrode during the charge/discharge of LICs.

At this point, it is essential to highlight a remarkable contribution by Levi et al. [14], which addresses the charge exchange processes occurring at an AC electrode operating in an extended potential range, as observed during the charge/discharge of a LIC. In this reference, *operando* Electrochemical Quartz Crystal Microbalance (EQCM) was used during cyclic voltammetry between 1.8 and 4.2 V *vs.* Li/Li^+ to investigate the compositional changes induced by the polarization of a microporous activated carbon electrode in contact with 0.1 mol L^{-1} $LiBF_4$ in propylene carbonate (PC) [14]. Interestingly, comparing EQCM results with the calculated mass changes of the AC electrode under negative polarization relative to the *PZC* led to the conclusion that

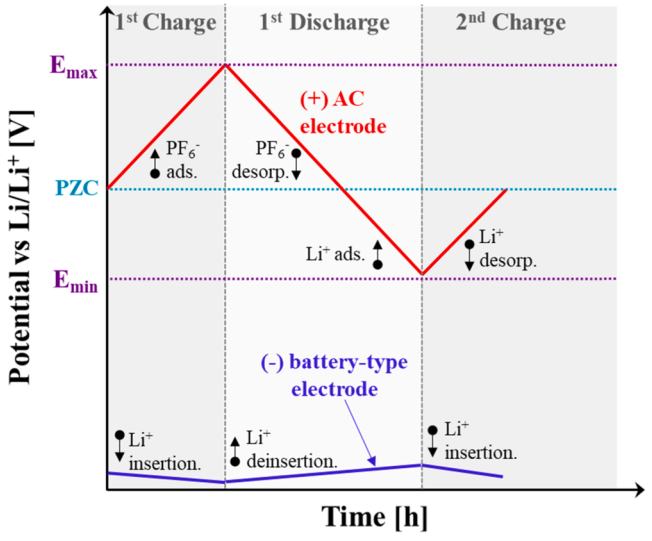

Fig. 1. Schematic galvanostatic profiles of the electrodes (adapted from ref. [13]) during the first charge/discharge sequence of a LIC in $LiPF_6$-based electrolyte after the prelithiation of the negative electrode. The red and blue lines represent the potential profile of the positive and negative electrodes, respectively.

lithium cations are not completely stripped of their solvation shell, which in the bulk electrolyte consists of 4 PC molecules [15]. Instead, they are accompanied by only 3 PC molecules within the electrode porosity. A similar comparison under positive polarization of the AC electrode relative to the *PZC* revealed that BF_4^- anions are poorly solvated when they are electrosorbed. This observation agrees with the fact that the energy cost of stripping BF_4^- ions from the PC molecules is about ten times smaller than that for $Li^+(PC)_4$ [16]. Nonetheless, the appearance of a cathodic peak below 2.0 V *vs.* Li/Li^+ in the cyclic voltammogram obtained with the $LiBF_4$-based electrolyte in ref. [14] suggests that the corresponding experiment was conducted slightly out of the *ESW* of the electrolyte. The presence of such a faradaic signature reveals the formation of decomposition products, which could perturb the charge exchange processes at the electrode. Therefore, for better accuracy, such *operando* analysis on an AC electrode should preferably be conducted within the stability potential window.

Given the context, we aim to determine how the positive AC electrode of LICs could reduce their life span. Therefore, this study intends to elucidate the ion population changes in an AC electrode operating within an extended potential range, akin to the positive electrode of a LIC in an organic electrolyte during its charge/discharge. To achieve this objective, experiments were conducted on AC electrodes immersed in 1 mol L^{-1} lithium hexafluorophosphate in a 1:1 (v/v) mixture of ethylene carbonate and dimethyl carbonate, using metallic lithium as a reference/counter electrode. To avoid the detrimental effects of parasitic faradaic reactions, we first determined the stability limits (E_{min} and E_{max}, minimum and maximum potential limits) of the selected electrolyte by using a window opening method [17]. Subsequently, to correlate variations in AC electrode properties with changes in ion population, we applied *operando* electrochemical dilatometry (ECD), *in situ* potentiostatic electrochemical impedance spectroscopy (PEIS), and *operando* Raman spectroscopy, while sweeping from the open circuit potential (*OCP*) to E_{max}, then from E_{max} to E_{min}, and finally from E_{min} to E_{max}. The general changes disclosed in the literature on AC electrodes polarized in organic electrolytes are confirmed, yet with new features. The most noticeable features are desorption peaks (appearing with greater polarization than adsorption) attributed to populations of PF_6^- anions and Li^+ cations trapped in difficult-to-access pores during anodic and cathodic scans, respectively. The reasons for these trapping phenomena, which were not disclosed for EDLC electrodes and are essentially due to the extended operating range of the AC electrode, are deeply discussed in light of our various *operando/in situ* investigations. It is anticipated that they accelerate the ageing of the AC electrode during the cycling of LICs, and consequently are essentially responsible for their reduced life span as compared to EDLCs.

2. Experimental

2.1. Materials

The material chosen for the EDL working electrodes (WE) was activated carbon YP-50F (Kuraray), hereafter referred to as AC throughout the manuscript. To rule out the presence of surface functional groups that could induce redox reactions during electrochemical testing, the AC sample was analyzed using a Thermo Scientific™ FlashSmart Elemental Analyzer. The results revealed that the material contains 1.44 wt.% oxygen, 0.41 wt.% hydrogen, 0.1 wt.% nitrogen, and 0 wt.% sulfur. The low oxygen content was further confirmed by temperature-programmed desorption (TPD) using a thermogravimetric analyzer (TG209 F1 Iris, NETZSCH) coupled to a mass spectrometer (QMS 403C Aëolos, NETZSCH). In the TPD run, approximately 6 mg of the powdered sample was heated to 900 °C at a rate of 10 °C per minute under a helium flow of 50 mL min^{-1}. This experiment confirmed that the AC contains less than 1.5 wt.% oxygen. AC-based electrodes were prepared by physically mixing 90 wt.% AC, 5 wt.% polytetrafluoroethylene binder (PTFE; 60 wt.% dispersion in water, Merck), and 5 wt.% carbon black (C-nergy

Super C65, Imerys) along with a small amount of 2-propanol (99.7 %, Avantor) in a mortar for approximately 40 minutes. The resulting dough-like material was shaped into an electrode sheet, which was then calendered between two polyethylene films until a thickness of approximately 100 μm was achieved. Disc electrodes (with diameters of 10, or 18 mm) were cut from the sheet using hollow punchers (FACOM) and subsequently dried under vacuum at 120 °C for 12 h in a Büchi B-585 drying oven. The nitrogen adsorption/desorption isotherm of the AC electrodes at 77 K (**Figure S1a** in the *Electronic Supplementary Information - ESI*) is of type I characterized by a steep increase at low relative pressure and a well-defined "knee" followed by a plateau, indicating that the material mostly exhibits micropores [18]. The 2D-NLDFT pore size distribution (PSD) [19] in **Figure S1b** of the *ESI* reveals that the porosity extends up to approximately 2.4 nm. Roughly 90% of the total pore volume is due to micropores (**Table S1** in the *ESI*), which are generally beneficial for the capacitive performance of the electrodes.

The electrolyte utilized in this work consisted of 1 mol L^{-1} lithium hexafluorophosphate ($LiPF_6$, anhydrous, Acros Organics) in a 1:1 (v/v) mixture of ethylene carbonate (EC, anhydrous, 99%, Millipore Sigma) and dimethyl carbonate (DMC, anhydrous, 99.7%, Millipore Sigma), hereafter referred to as "$LiPF_6$/EC:DMC". Coulometric Karl Fischer titration of the electrolyte, using an 831 KF Coulometer (Metrohm), gave a low water content value of 14 ppm.

Lithium metal ribbon (99.9% trace metals basis, Millipore Sigma) was used as the counter/reference electrode (CE/RE).

2.2. Cells assembly and electrochemical investigations

The electrochemical stability window (*ESW*) and point of zero charge (*PZC*) of the AC electrodes in the $LiPF_6$/EC:DMC electrolyte were determined in 3-electrode ECC-ref cells (EL-CELL). The cells were assembled with an AC working electrode (WE; diameter = 18 mm), a lithium metal disc as the counter electrode (diameter = 18 mm), and a glass fiber separator (Whatman GF/D, 670 μm thick) soaked in electrolyte. A reference electrode made of a lithium metal pin was placed between the working and counter electrodes. The determination of *ESW* was conducted by cyclic voltammetry (CV) in potential regions either lower or higher than *OCP* (Open Circuit Potential of approximately 3.05 V *vs.* Li/Li^+) in distinct cells, with stepwise adjustments (in 100 mV steps) to the reductive or oxidative potential limits, respectively. It is crucial to note that the CVs were recorded at a low scan rate of 1 mV s^{-1} to precisely identify faradaic processes resulting from electrolyte decomposition within the examined potential range. The *PZC* was determined as the potential corresponding to the lowest capacitive current in cyclic voltammograms (CV) recorded at a scan rate of 1 mV s^{-1} from 2.2 V to 3.5 V *vs.* Li/Li^+. The *PZC* was also identified by Staircase Potentiostatic Electrochemical Impedance Spectroscopy (SPEIS), where Nyquist plots were generated at constant potentials (separated by 100 mV) in the range from 2.2 V to 3.5 V *vs.* Li/Li^+ by applying a sinusoidal signal of 5 mV s^{-1} over the frequency range from 100 kHz to 10 mHz. The specific capacitance (C_{EIS}, [F g^{-1}]) was determined by applying Eq. (1) [20]:

$$C_{EIS} = \frac{1}{2\pi * f * -Im(Z) * m} \quad (1)$$

where f [Hz] is the frequency, $-Im(Z)$ [Ohm] is the imaginary component of the impedance, and m [g] is the active mass of the AC electrode. The *PZC* was determined by identifying the lowest capacitive element on the Nyquist plots.

Operando electrochemical dilatometry (ECD) measurements were performed using an ECD-3-nano dilatometer (EL-CELL), which operative principle is shown in **Figure S2** of *ESI*. The cell assembly consists of two electrodes separated by a rigid glass T-frit (upper/lower diameter of 10/12.5 mm, respectively, thickness of 6.3 mm) fixed-in-position. The AC working electrode (diameter = 10 mm, thickness ≈ 100 μm) is placed on top of the T-frit and surmounted by a thin stainless-steel membrane (thickness = 50 μm) which transmits any change in WE height to a displacement transducer via a moveable plunger. A stainless-steel spacer disc (10 mm in diameter and 2.7 mm in thickness) is placed between the WE and the membrane to ensure electrical contact; it is important to note that the load exerted by the spacer on the WE was approximately 1 N. The counter electrode (CE) placed under the T-frit was a lithium metal disc (diameter = 12 mm) covered by a glass fiber separator (Whatman GF/A, 260 μm thick). Both the glass fiber separator and the T-frit were impregnated with approximately 500 μL of the $LiPF_6$/EC:DMC electrolyte. A lithium metal pin located at mid-height of the T-frit was used as the reference electrode to monitor the potential changes of the AC electrode. Following the assembly, the dilatometer was housed in a climatic chamber (Suszarka SML, Zalmed) to maintain a constant cell temperature of 295 K during the electrochemical measurements. The changes in AC electrode thickness were recorded during cyclic voltammetry at 1 or 0.25 mV s^{-1} within the *ESW* of the electrolyte from 2.2 V to 4.5 V *vs.* Li/Li^+.

Operando Raman spectroscopy during cyclic voltammetry was performed with an EQ-STC-RAMAN split test cell (MTI Corporation), using an AC working electrode (diameter = 10 mm) placed behind a quartz window, and a lithium metal disc as counter/reference electrode (diameter = 12 mm), with both sandwiching a glass fiber separator (Whatman GF/D, 670 μm thick) soaked with the $LiPF_6$/EC:DMC electrolyte. The spectra were collected at specific potential values between 2.2 V and 4.5 V *vs.* Li/Li^+ during cyclic voltammetry at 0.25 mV s^{-1} (in such conditions a Raman spectrum was recorded within 90 s), using a Raman microscope (ThermoFisher Scientific®) equipped with a custom holder for precise adjustment of the AC electrode. A HeNe laser with a wavelength of 632.8 nm served as the excitation source. To prevent significant heating of the AC electrode, the laser power was reduced to 3 mW. To ensure a good signal-to-noise ratio, each spectrum was obtained after accumulating 9 scans of 10 s. The Raman spectra were deconvoluted blindly using a Gaussian fitting function through the peak analyzer tool available in Origin v9.65; the I_{D1}/I_{G1} intensity ratio was calculated using the fitted peaks areas (so-called integrated intensities) [21].

In situ potentiostatic electrochemical impedance spectroscopy (PEIS) was performed in the same cell and configuration used for Raman measurements. Nyquist plots were generated at selected potential values during cyclic voltammetry at a scan rate of 0.25 mV s^{-1} within 2.2 V to 4.5 V *vs.* Li/Li^+ using a sinusoidal signal of 5 mV s^{-1} over the frequency range from 100 kHz to 1 Hz; each PEIS measurement lasted approximately 26 seconds. Due to the short duration of the impedance measurements, the current response during cyclic voltammetry remained largely unaffected. This approach aimed to determine the ionic resistance ($R_{ionic;}$ associated with the diffusion of ions in the porosity) at various potentials of the AC electrode [22]. Notably, the equivalent series resistance (*ESR*) and the charge transfer resistance (R_{CT}) remained constant during the measurements. The EC-lab v11.40, using the Module Bat, was utilized to alternately execute cyclic voltammetry and impedance measurements. Subsequently, the Z-fit tool within the EC-lab v11.40 was then used to analyze the Nyquist plots and determine R_{ionic}.

The cells employed in this study were assembled in an argon-filled glove box (Workstation Unilab Pro, MBraun) with O_2 and H_2O levels lower than 1 ppm. All the electrochemical investigations on AC electrodes were performed with a VMP3 electrochemical workstation (Bio-Logic).

2.3. Computational methods

Molecular dynamics (MD) simulations were conducted to scrutinize the local structure of the $LiPF_6$/EC:DMC electrolyte both in the bulk and inside the porosity of a model porous carbon without applied charge. The porous carbon used as the electrode in the simulations was generated by Quench Molecular Dynamics simulations using ReaxFF as the

reactive force field to model the interactions, breaking, and formation of chemical bonds between carbon atoms, as outlined in reference [23]. Briefly, the initial system consisted of 2500 carbon atoms randomly placed in a 59 nm^3 cubic box at 2100 K. This choice of initial temperature represents a pyrolysis process after the polymer chains break down and most other elements (oxygen, hydrogen, …) are evolved. Periodic boundary conditions were applied in all three directions to avoid edge effects. The system was then gradually quenched to 295 K over 140 ps while keeping a constant volume. Due to the high initial temperature, a small time step of 0.07 fs was necessary to avoid problems in the integration of Newton's equation. As the temperature decreased, carbon atoms started to aggregate and form a porous texture. After quenching, any isolated carbon atoms are removed. The nitrogen adsorption isotherm of the model porous carbon at 77 K was simulated using the software RASPA [24], and its textural properties were determined with the 2D-NLDFT approach [19] employed to analyze the AC. It is interesting to note that the pore size distribution and textural properties of this carbon shown in **Figure S3b** and **Table S2** of *ESI* do not differ significantly from the features of the YP-50F powder shown in **Table S2** in the *ESI*.

To mirror the composition of the $LiPF_6$/EC:DMC electrolyte in the model porous carbon, the latter was placed in a fixed position as a rigid body in the middle of a 909 nm^3 parallelepiped box, housing 225 Li^+ cations, 225 PF_6^- anions, 1638 EC, and 1300 DMC molecules. The initial positions of the electrolyte molecules were generated using the Packmol software [25]. The GROMOS 54A7 force field [26] was used to accurately replicate the interatomic interactions in the electrolyte throughout the calculation, while the LAMMPS MD package [27] simulated the molecular movements at constant pressure (1 bar), temperature (295 K), and number of molecules (NPT ensemble), using periodic boundary conditions throughout the simulation. The temperature of the system was regulated using a Nosé-Hoover thermostat with a time constant of 10 fs. The system underwent equilibration for 50 ns, allowing the electrolyte to penetrate the porosity of the model porous carbon, while attaining density values (1.30 g mL^{-1}) close to the experimentally measured ones for the bulk solution. After reaching equilibrium, the atomic coordinates were collected for an additional 10 ns at intervals of 0.1 ps for analyzing the local structure of the electrolyte both inside and outside the porosity of the model carbon during the simulation time. This last part is required to analyze the radial distribution function for various atomic pairs. The atomic positions at each time step were scrutinized using the OVITO software [28].

3. Results and discussion

3.1. Properties of the $LiPF_6$/EC:DMC electrolyte in a porous carbon electrode

As stated in the introduction, to appropriately address the ion population changes within the pores of the positive AC electrode of a LIC, it is essential to first establish the stability limits of this electrode before conducting any *operando* and/or *in situ* analysis. Therefore, the potential range within which the $LiPF_6$/EC:DMC electrolyte is stable on a porous AC electrode (also called the electrochemical stability window - *ESW*) during the electrochemical experiments has been determined by the window opening method [17]. It involves recording cyclic voltammograms (with a low scan rate of 1 mV s^{-1}) at potentials either lower or higher than the open circuit potential (*OCP*) of approximately 3.05 V *vs.* Li/Li^+, while decreasing or increasing the vertex potential by steps of 0.1 V, respectively. Subsequently, the coulombic efficiency is calculated from the voltammograms recorded at a potential lower (CE_{neg}) and higher (CE_{pos}) than *OCP*, according to Eqs. (2) and (3), respectively [29]:

$$CE_{neg} = \frac{Q_{Anodic}}{Q_{Cathodic}} \quad (2)$$

$$CE_{pos} = \frac{Q_{Cathodic}}{Q_{Anodic}} \quad (3)$$

where Q_{Anodic} and $Q_{Cathodic}$ are the anodic and cathodic capacities, respectively, obtained by integrating the respective parts of the CVs. In the plots of coulombic efficiency versus vertex potential (Fig. 2), the coulombic efficiency values are close to 1 within the potential range from 2.2 V and 4.5 V *vs.* Li/Li^+, defining the *ESW* of the $LiPF_6$/EC:DMC electrolyte on the AC electrode. Beyond these limits, the efficiency decreases dramatically due to reductive or oxidative faradaic reactions.

The local structure of the electrolyte, both in its bulk state and within the porosity of the model carbon, was determined using molecular dynamics (MD) simulations without applied polarization. The objective was to examine changes in anion and cation solvation shells as they penetrate the porosity, providing support for interpreting the electrochemical dilatometry measurements. The radial distribution functions of the $LiPF_6$/EC:DMC electrolyte obtained in both its bulk state and within the porosity of the model carbon are shown in Figs. 3**a** and 3**b**, respectively. These functions, denoted *g(r)*, represent the probability of finding two atoms at a distance *r* compared to the same probability in a perfectly homogeneous system. In Fig. 3**a**, the radial distribution functions for the pairs constituted by lithium cations and oxygen atoms of the carbonyl groups from EC and DMC molecules (Li^+ - O_{EC} and Li^+ - O_{DMC}, respectively) show a narrow peak at ca. 2.6 Å. This indicates a well-defined solvation shell with the presence of both types of carbonate molecules. Interestingly, the first peak corresponding to the most probable distance between lithium and phosphorous from PF_6^- anions (Li^+ - PF_6^-) is observed at around 3.5 Å. This suggests that the counter-ion is present within the solvation shell of the cation. A different trend is seen for the phosphorous from PF_6^- anions and carbon atoms from the EC and DMC molecules (PF_6^- - C_{EC} and PF_6^- - C_{DMC}, respectively), where the peaks are broader and less pronounced, suggesting that solvent molecules dynamically move in and out of the first solvation shell of the PF_6^- anions on a short time scale, indicating the absence of a well-defined first solvation shell, which is consistent with the results presented in reference [30]. Inside the porosity of the model carbon (Fig. 3**b**), the peaks for the Li^+ - O_{DMC} and Li^+ - PF_6^- pairs are sharper and exhibit higher intensities compared to those outside the porosity. This suggests that DMC molecules and PF_6^- anions have a relatively higher presence in the solvation shell of the cation, whereas, the radial distribution of other atomic pairs

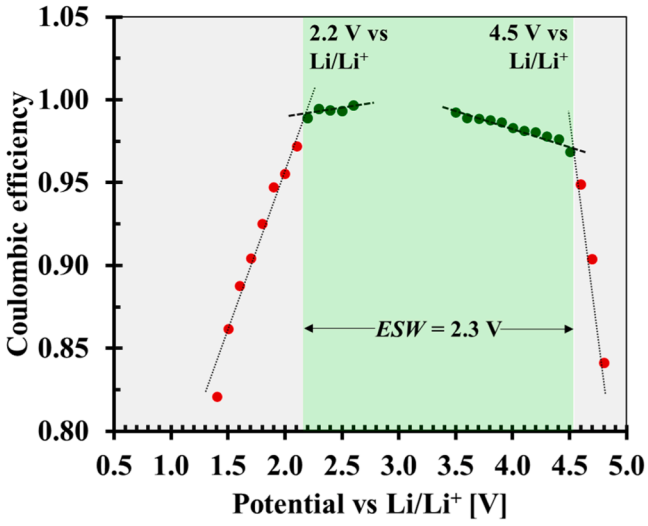

Fig. 2. Plots of coulombic efficiency versus vertex potential from window opening realized on an AC electrode in the $LiPF_6$/EC:DMC electrolyte at potentials lower or higher than *OCP*. Data points are represented as dark green dots in the stability region of the electrolyte, and red dots where faradaic reactions occur.

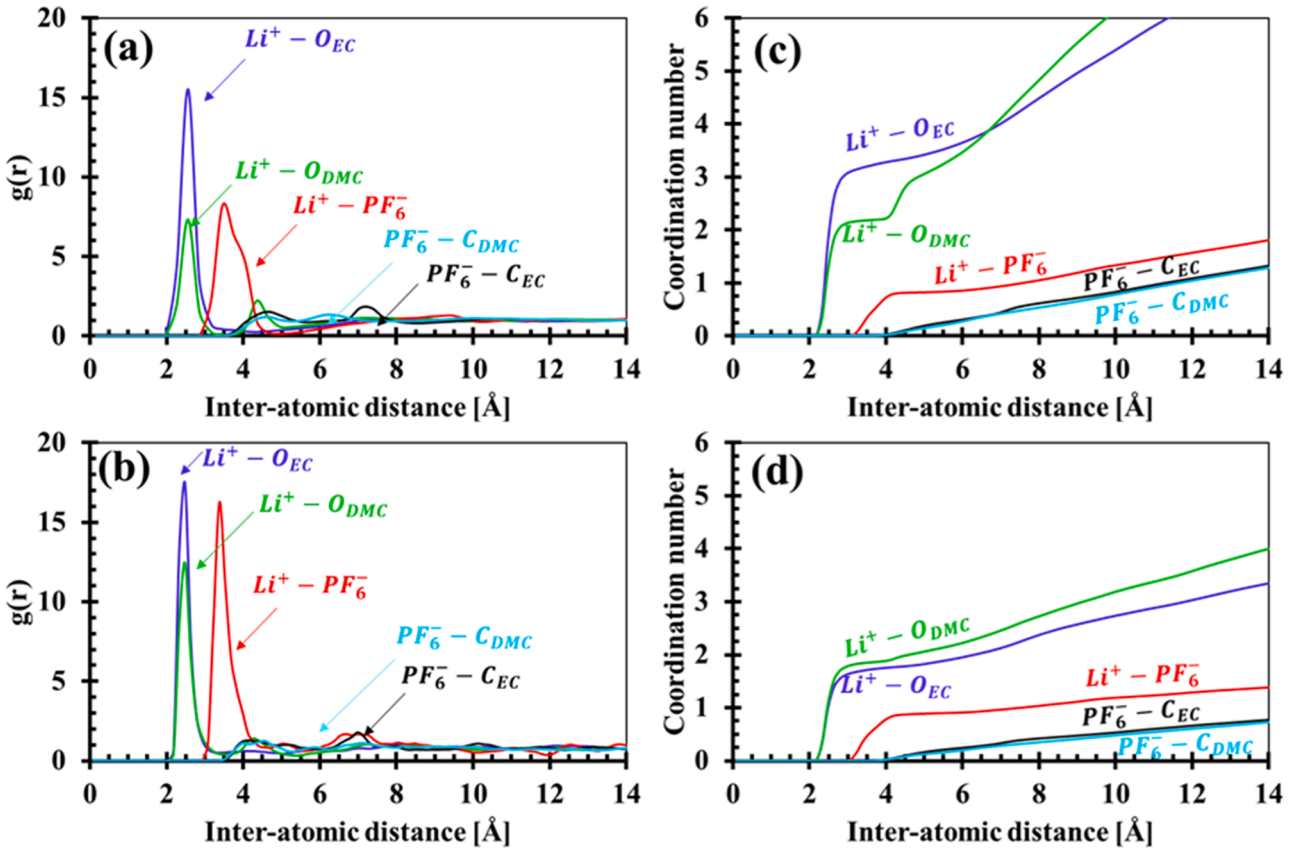

Fig. 3. Analysis of the local structure of the $LiPF_6$/EC:DMC electrolyte from MD simulations: (a) and (b) Radial distribution functions for the bulk solution and inside the porosity of a model porous carbon, respectively; (c) and (d) Cumulative coordination number versus inter-atomic distance for the bulk solution and inside the porosity of model porous carbon, respectively. Color code: (i) Li^+ - O_{EC} (blue line); (ii) Li^+ - O_{DMC} (green line); (iii) Li^+ - PF_6^- (red line); (iv) PF_6^- - C_{EC} (black line) and PF_6^- - C_{DMC} (turquoise line).

remains virtually unchanged.

The coordination number (CN(*r*)) has been calculated using Eq. (4):

$$CN(r) = 4\pi\rho \int_{r_{min}}^{r_{max}} g(r) r^2 \, dr \tag{4}$$

where ρ is the volume number of the atoms of interest, r_{max}, and r_{min} denote the maximum and minimum distance to define the range of space analyzed, and *g(r)* is the pair distribution function between the central atom/ion and the solvating species. The cumulative coordination number as a function of interatomic distance for both the bulk of the solution and within the porosity of the model carbon is presented in Figs. 3**c** and 3**d**, respectively. This representation enables one to ascertain that the solvation shell of Li^+ in the bulk of the electrolyte consists of 3 EC molecules, 2 DMC molecules, and 1 PF_6^- anion, whereas inside the model carbon's porosity, the lithium cation has lost 1 EC molecule from its solvation shell. Notably, the PF_6^- anions are not accompanied by any solvent molecule, either in the bulk solution or inside the porosity of the model carbon. This analysis of local structure reveals the existence of contact ion pair (CIP) interactions, which may be due to the limited screening effectiveness of the solvent, consistent with the observations in the ionic pairs from $LiClO_4$-based electrolyte reported in ref. [31]. Following the coordination analysis, the dimensions of clusters formed due to Li^+ solvation were measured, both within and outside the porosity of the model porous carbon. The average diameters of the clusters (**Figure S4** of *ESI*) were found to be approximately 0.96 nm and 1.26 nm, respectively.

3.2. Identification/attribution of ion population changes in the EDL-positive electrode of a LIC

Several studies, such as *operando* electrochemical quartz crystal microbalance (EQCM) or electrochemical dilatometry (ECD), and *in situ* nuclear magnetic resonance (NMR), have aimed to categorize ion population changes within porous carbon electrodes in EDLCs into different domains based on the applied potential [14,32,33,34]. For this purpose, there is an important emphasis on determining the point of zero charge (*PZC*) of the porous carbon electrode, viz, the potential where the electrode net surface charge is zero ($Q = 0$) [34]. This determination is crucial for drawing the electrostatic separation between the electrosorption of anions and cations as the potential is swept positively and negatively relative to the *PZC*, respectively [14]. In this study, the *PZC* of an AC electrode in the $LiPF_6$/EC:DMC electrolyte was determined *vs.* a lithium metal counter/reference electrode using cyclic voltammetry (CV) at 1 mV s^{-1} (Fig. 4**a**) and staircase potentiostatic electrochemical impedance spectroscopy (SPEIS) (Fig. 4**b**). In Fig. 4**a**, the voltammogram of the AC electrode exhibits a characteristic butterfly shape [35], indicative of a capacitive charge storage mechanism within the selected potential range. The *PZC* was identified at the minimum value of the capacitive current in the CV, i.e., 2.9 V *vs.* Li/Li^+. Similarly, a minimum of capacitance (calculated using Eq. (1)) was observed at 2.9 V *vs.* Li/Li^+ in the plot of capacitance *vs.* fixed potential (Fig. 4**b**) obtained from SPEIS. Notably, the same *PZC* value was found in other types of electrochemical cells, as shown in **Figure S5** of *ESI*. All the CV and ECD curves further presented in this manuscript will be referred to the *PZC* value of 2.9 V *vs.* Li/Li^+.

Operando electrochemical dilatometry (ECD) plots, obtained on an

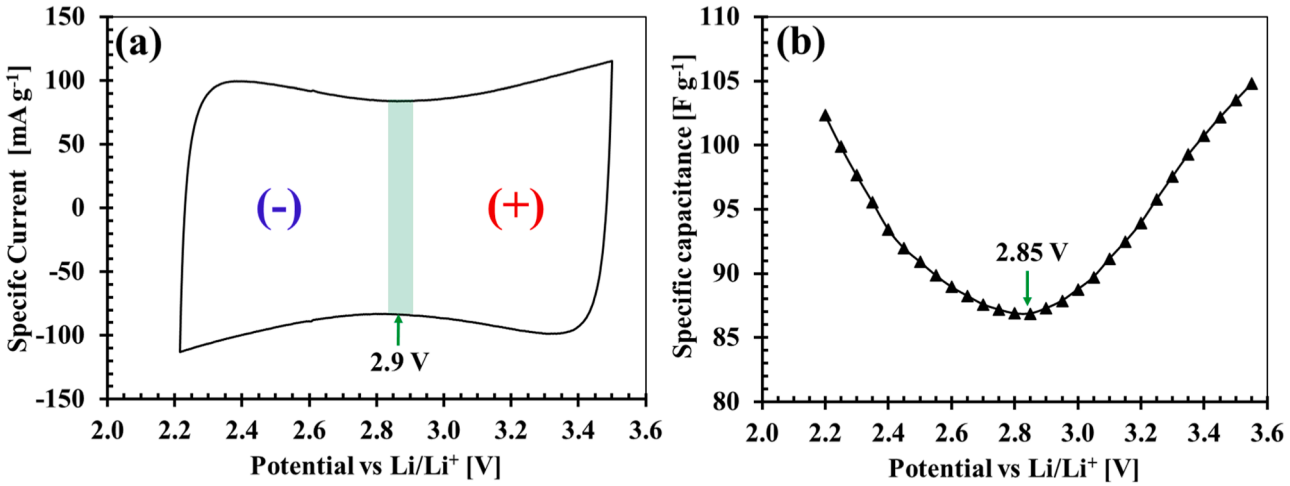

Fig. 4. Determination of the point of zero charge (*PZC*) of an AC electrode in the $LiPF_6$/EC:DMC electrolyte: (a) by cyclic voltammetry at a scan rate of 1 mV s^{-1} and (b) from the capacitance values extracted from Nyquist plots obtained from SPEIS.

AC electrode positively polarized relative to *PZC* in various potential ranges, are presented in Fig. 5. The cyclic voltammograms (at 1 mV s^{-1}) in Fig. 5**a** were recorded with increasing vertex potentials in 100 mV steps while staying within the *ESW*; Fig. 5**b** displays the corresponding changes in electrode height. During the anodic scans, the capacitive response of the electrode increases with the potential, as expected for EDL behaviour (see Fig. 5**a**). Notably, up to a vertex potential of 3.5 V *vs.* Li/Li^+, the electrode height remains virtually unchanged, as shown in the inset of Fig. 5**b**. This stability in height suggests that ionic exchange occurs within this potential region, where anions are attracted, and cations are expelled to balance the increasing positive charge density, a trend observed in EQCM studies with organic electrolytes [14,32,36]. Beyond the E_{max} limit of 3.5 V *vs.* Li/Li^+, the electrode height in Fig. 5**b** increases more rapidly with the change of vertex potential. This rapid rise is attributed to the completion of ionic exchange and the onset of exclusive anion adsorption on the electrode surface, i.e., once the evacuation of cations is completed, and the potential is high enough, some less accessible pores can be occupied by anions. Notably, bare PF_6^- anions likely penetrate the electrode porosity during anion adsorption due to their weakly bound and poorly defined first solvation shell, as suggested by MD simulations and depicted in Fig. 3**d**. This is further supported by the observation that the AC electrode reaches a maximum height change of 0.81% at 4.5 *vs.* Li/Li^+ (see Fig. 5**b**), closely matching the 0.80% observed for a YP17-based electrode in $EMImBF_4$ (1-Ethyl-3-methylimidazolium tetrafluoroborate) at the same potential [37], with the bare BF_4^- anions having the same diameter as the bare PF_6^- (see **Figure S1b** in the *ESI*). During the cathodic scans, the capacitive current decreases, following the expected trend for EDL behaviour (Fig. 5**a**), while the rapidly decreasing height down to ca. 3.5 V *vs.* Li/Li^+ followed by an almost constant height down to the *PZC* (Fig. 5**b**) are the signatures of PF_6^- anions desorbing in significant amounts followed by ionic exchange. Notably a (growing) peak with a minimum located ca. 3.2 V *vs.* Li/Li^+ is observed in the CVs recorded with vertex potentials higher than 3.8 V *vs.* Li/Li^+ during the anodic scans (Figs. 5**a**). This relatively small peak is attributed to the desorption of PF_6^- anions trapped in poorly accessible micropores of the AC electrode; in other words, some PF_6^- anions may be drawn in these pores when the potential is sufficiently high during the anodic scans. However, the liberation of these trapped anions during the cathodic scan requires applying a lower potential than the anodic one necessary for their penetration. Noteworthy, during the cathodic scans, the point of minimum height (*PMH*) of the electrode is reached around 3.1 V *vs.* Li/Li^+ (see the inset in Fig. 5**b**), which is lower

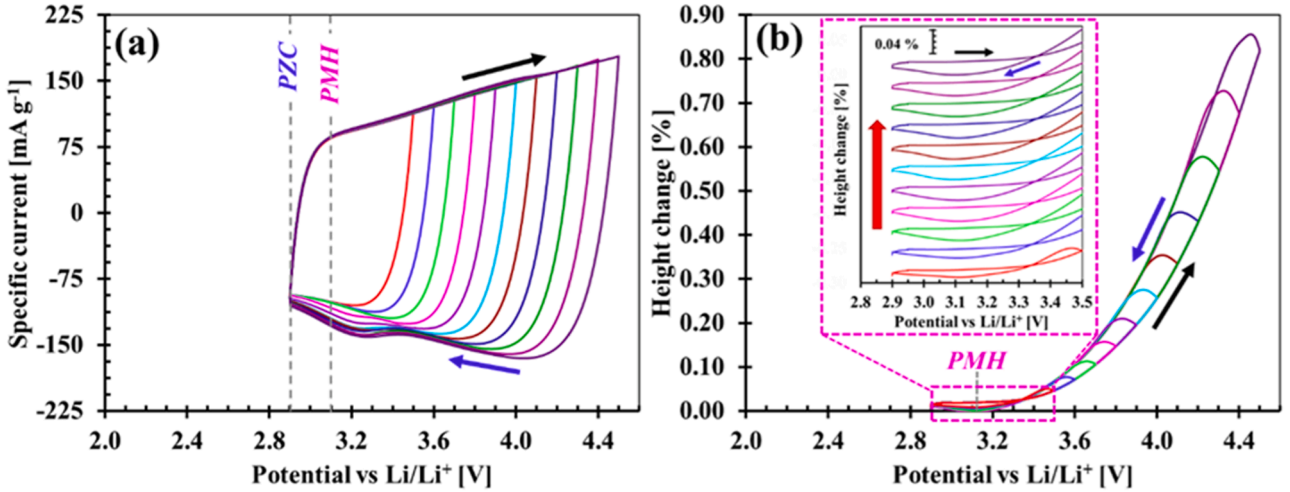

Fig. 5. *Operando* electrochemical dilatometry (ECD) on an AC electrode polarized positively relative to *PZC*: (a) Cyclic voltammograms (at 1 mV s^{-1}) with vertex potentials increasing by steps of 0.1 V and (b) corresponding height changes, where the inset shows a stack of expanded dilatometric profiles in the potential range from 2.9 to 3.5 V *vs.* Li/Li^+ (with the red arrow indicating the shift direction). The black and blue arrows display the progression of the anodic and cathodic scans, respectively. *PZC* is the point of zero charge and *PMH* is the point of minimum height. The electrolyte is $LiPF_6$/EC:DMC.

than the electrode height during the anodic scans, implying that the anion flux-out exceeds slightly the cation flux-in, allowing for a small contraction of the electrode in this potential range. Since this *PMH* corresponds in Fig. 5**a** with the end of the peak attributed to desorption of trapped PF_6^- anions at 3.1 V *vs.* Li/Li^+, it indicates that the ionic exchange phenomenon is complete at this potential. Consequently, the slight height increase from *PMH* to *PZC* indicates the perm-selective adsorption of some cations to compensate for the charge of the electrode.

In the next step of the ECD investigations, the AC electrode in the $LiPF_6$/EC:DMC electrolyte was polarized between $E_{min} = 2.2$ V *vs.* Li/Li^+ (the limit of electrolyte reduction, see Fig. 2) and E_{max} vertex potentials varying in steps of 0.1 V from 3.5 V to 4.5 V *vs.* Li/Li^+ (the limit of electrolyte oxidation, see Fig. 2). This sequence was applied to characterize the effect of cycling the electrode within the real potential range observed for the positive electrode of a LIC. During the cathodic scan, when the electrode is polarized from *PZC* down to 2.2 V *vs.* Li/Li^+, the perm-selective adsorption drawing cations from the bulk electrolyte into the porosity of the electrode takes place [32,36], while some anions remain within the porosity.

When the electrode was anodically polarized between 2.2 V *vs.* Li/Li^+ and the various potential limits E_{max}, the general trend in the part of CVs at a potential higher than *PZC* was an increase in capacitive current (Fig. 6**a**), while the height of the electrode began increasing for E_{max} vertex potentials higher than 3.5 V *vs.* Li/Li^+ (Fig. 6**d**), similarly to that case analyzed in Fig. 5, which could indicate a similar mechanism, with ionic exchange followed by anion adsorption. This apparent similarity in the anodic mechanism was confirmed during the subsequent cathodic scans down to the *PZC,* where the peak at 3.2 V *vs.* Li/Li^+, associated with the release of anions, progressively grew as the anodic vertex potential was extended (see Fig. 6**b** and 6**c**), whilst the height of the electrode decreased until reaching the *PMH* at around 3.1 V *vs.* Li/Li^+ (Fig. 6**d**). Interestingly, when the AC electrode was firstly polarized down to 2.2 V *vs.* Li/Li^+, one could observe during the anodic scans (Fig. 6**b**) an emerging peak with a maximum at approximately 3.8 V *vs.* Li/Li^+, which was not previously observed in Fig. 5**a** when the electrode was solely polarized at potential higher than the *PZC*. This peak likely results from the desorption of Li^+ cations trapped in poorly accessible pores during the preceding cathodic scan. Such adsorbed ions can be effectively released from their potential well through electrochemical driving forces, specifically by applying sufficiently high anodic polarization. A similar phenomenon of cation trapping in the negative electrode of an EDLC and its liberation by applying a much higher potential has been reported with 1 mol L^{-1} $TEABF_4$ in propylene carbonate [38].

The complete cyclic voltammogram and related volumetric profile of a fresh AC electrode in the $LiPF_6$/EC:DMC electrolyte are shown in Figs. 7**a** and 7**b** within the maximum potential range (i.e., from 2.2 to 4.5 V *vs.* Li/Li^+). During the first anodic scan from *OCP* to 4.5 V *vs.* Li/Li^+ (green line), the current response of the electrode increased similarly to that of a positive electrode in an EDLC. Interestingly, the *OCP* of 3.1 V *vs.* Li/Li^+ corresponds to the *PMH* identified in Fig. 5**a** as the end of the exchange of perm-selectively adsorbed cations with anions. Therefore, the small increase in height up to 0.09% at 3.8 V *vs.* Li/Li^+ corresponds to the exchange of naturally adsorbed cations with PF_6^- anions. Then, as the potential increased from 3.8 V *vs.* Li/Li^+, the height of the electrode increased rapidly up to 0.9% at 4.5 V *vs.* Li/Li^+, indicating that the adsorption of anions took place. During the cathodic scan down to the *PZC* (purple lines in Fig. 7), the trend was the same as in Fig. 5, i.e., the capacitive current decreased, yet with a broad peak superimposed at approximately 3.2 V *vs.* Li/Li^+ characterizing the release of trapped PF_6^- anions. In parallel, the steady decrease of electrode height down to approximately 3.4 V *vs.* Li/Li^+ and its almost constant value down to the *PZC* indicated significant desorption of PF_6^- anions followed by the ionic exchange process (ending at *PMH* of 3.1 V *vs.* Li/Li^+ as shown in Fig. 5). From 3.1 V *vs.* Li/Li^+ down to 2.2 V *vs.* Li/Li^+, the capacitive current was substantially smaller than at higher potentials, whereas the electrode thickness reached only 0.3% down to E_{min}. According to MD simulations (see Fig. 3**d**), it should be noted that lithium cations were not fully desolvated upon entering the electrode porosity, displaying an average diameter of approximately 0.96 nm (see **Figure S4c** in the *ESI*). Such a high diameter hinders the easy access of additional cations into the electrode porosity, contributing to the relatively low values of capacitive current and electrode expansion in this potential range. During the second anodic scan from E_{min} to *PMH* (mustard lines in Fig. 7), lithium cations were desorbed from the electrode with a decrease in height. As the scan was prolonged beyond *PMH*, the capacitive current rose significantly, with the appearance of a peak at approximately 3.8 V *vs.* Li/Li^+, which was linked to the desorption of lithium cations adsorbed in

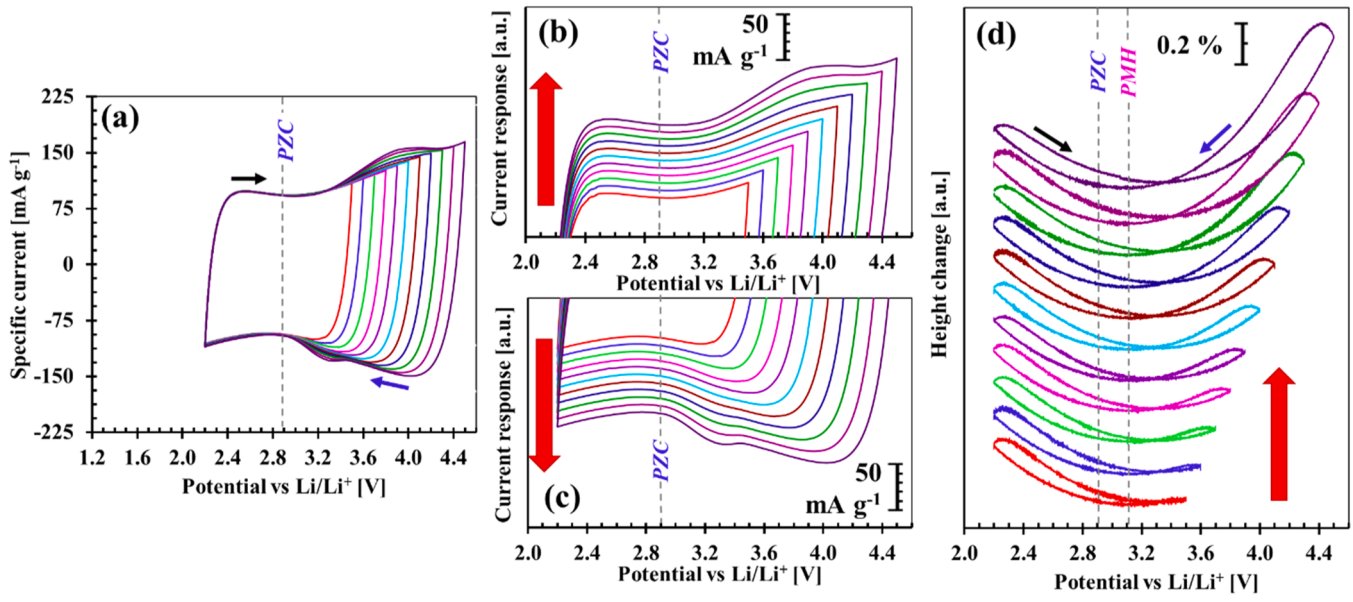

Fig. 6. *Operando* electrochemical dilatometry on an AC electrode cycled between 2.2 V *vs.* Li/Li^+ and various E_{max} vertex potentials varying from 3.5 V to 4.5 V *vs.* Li/Li^+ by steps of 0.1 V: (a) Cyclic voltammograms (CVs) recorded at a scan rate of 1 mV s^{-1}; (b) anodic and (c) cathodic CV scans shifted by a constant value of current; (d) stacked dilatometric profiles with an inset bar representing an expansion of 0.2%. The black and blue arrows display the progression of the anodic and cathodic scans, and the red arrows the shift direction. The electrolyte is $LiPF_6$/EC:DMC. *PZC* is the point of zero charge and *PMH* is the point of minimum height.

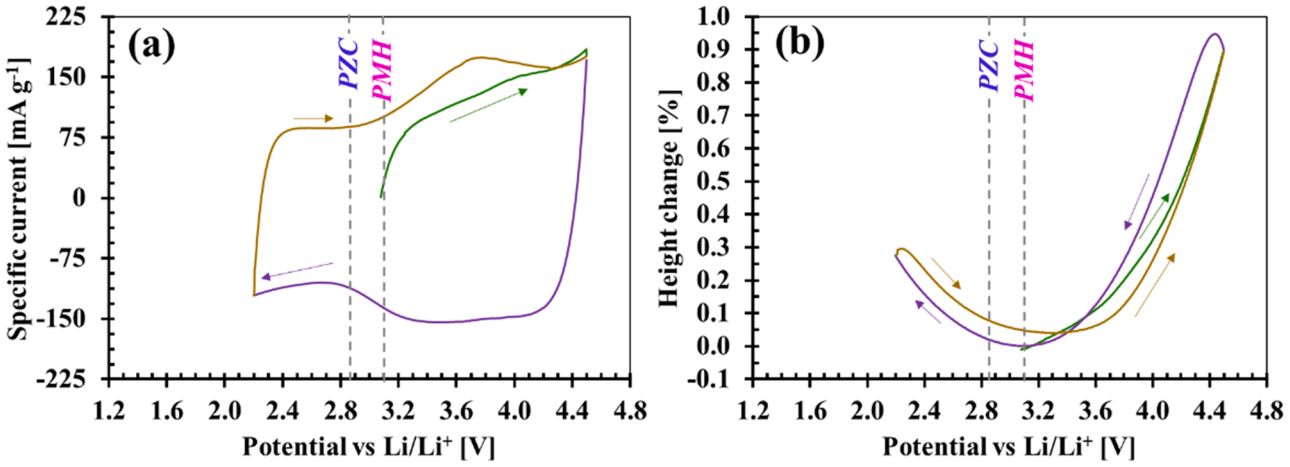

Fig. 7. (a) Cyclic voltammogram (at 1 mV s^{-1}) of a fresh AC electrode in 1 mol L^{-1} $LiPF_6$/EC:DMC starting from *OCP* and covering the potential range from 2.2 V to 4.5 V *vs.* Li/Li^+; (b) corresponding height changes of the electrode. The first anodic scan is represented by the green line, the first cathodic scan by the purple line, and the second anodic scan by the mustard line. *PZC* is the point of zero charge and *PMH* is the point of minimum height.

poorly accessible pores during the previous cathodic scan and remaining trapped until this potential was reached. In parallel, the nearly constant electrode thickness up to 3.8 V *vs.* Li/Li^+ indicated simultaneously an ionic exchange and the release of trapped lithium cations. Beyond 3.8 V *vs.* Li/Li^+, the sharp increase in electrode thickness up to approximately 0.9% was due to anion adsorption. This increasing strain can be paralleled with *in situ* atomic force microscopy (AFM) investigations on mesoporous porous membranes in 1-ethyl-3-methylimidazolium bis (trifluoromethylsulfonyl)imide, where a substantial increase in electrode thickness was observed upon prolonged accommodation of anions [39,40]. This provides extra confirmation that the origin of the strain observed in the porous AC electrode during positive polarization is related to the ion insertion into the pores.

3.3. Correlation of ionic transport and AC electrode structure with ion population changes

This section aims to correlate the changes in the in-pore ionic population during a potential scan, similar to the one presented in Fig. 7 for *operando* electrochemical dilatometry (ECD), while the changes in ionic transport were studied by *in situ* potentiostatic electrochemical impedance spectroscopy (PEIS), and the structural changes of the AC electrode were analyzed by *operando* Raman spectroscopy. Inspired by reference [41], which underscores that changes in ion population in the pores dominate the variations in in-pore ionic diffusion during charging an EDLC with tetraethylphosphonium tetrafluoroborate ($TEPBF_4$) in acetonitrile as the electrolyte, PEIS was employed to investigate the potential dependence of ionic resistance (R_{ionic} - also called Warburg impedance, determined according to the procedure shown in **Paragraph 5** of the *ESI*) arising from ion or molecule diffusion within the porous AC electrode material. On the other hand, as *operando/in situ* Raman spectroscopy had already proven to be instrumental in the study of EDLC electrodes [42-45], it was used to determine the evolution of the degree of disorder in the AC electrode by analyzing the I_{D1}/I_{G1} integrated intensity ratio after the deconvolution of spectra [21]. Additionally, interesting information about the effect of charge transfer on the stiffening/softening of C-C bonds in the AC electrode during polarization was obtained by analysis of the D2 band, in light of previous data obtained with doped single-wall carbon nanotubes [44]. **Figure S7** of the *ESI* depicts the potential values at which the Raman spectra were recorded, and the deconvolution of a few of them. To avoid significant shifts of potential in the AC electrode during the recording of the Raman spectra, a slow scan rate of 0.25 mV s^{-1} was imposed for all experiments of this section (in such conditions a Raman spectrum was recorded within 90 s).

The current response and the relative height changes of the AC electrode at a scan rate of 0.25 mV s^{-1} are depicted in Fig. 8**a,** where it is noteworthy that both parameters preserve the same characteristics as in Fig. 7, i.e., the capacitive response of the electrode in the potential region above *PZC* is significantly higher than below this potential, due to the shift in the operative mechanism. Moreover, the appearance of peaks associated with the liberation of trapped anions and cations during the first cathodic and second anodic scans, respectively, must be highlighted. The various types of in-pore ion population changes detailed in the foreword, and particularly in the comments of Fig. 7, are summarized at the top of Fig. 8**a**, with their potential domain of occurrence.

During the initial anodic polarization of the AC electrode (from *OCP* to 3.8 V *vs.* Li/Li^+) accompanied by ion exchange with a subtle increase in electrode thickness, there is a noticeable drop in R_{ionic} (Fig. 8**b**), suggesting that ionic diffusion within the AC porosity increases with the electrode potential. Such a tendency could be explained by considering that the electrode thickness is mostly controlled by in-pore ion population changes, which are strongly influenced by in-pore ionic diffusion, as demonstrated in ref. [41]. The constant I_{D1}/I_{G1} ratio in this potential range (Fig. 8**c**) reveals an unchanged number of defects, fitting well with the almost constant electrode height. Nonetheless, the D2 band related to defect scattering and reflecting the coexistence of sp^2 and sp^3 hybridized carbon atoms [46] slightly upshifts from 1330 to 1340 cm^{-1}, due to the increase in charge carriers' density (hole injection) provoked by the anodic polarization of the AC electrode. From 3.8 to 4.5 V *vs.* Li/Li^+, R_{ionic} continues to decrease (see Fig. 8**b**) due to the prior evacuation of partially solvated lithium cations during the ionic exchange, which allows the PF_6^- anions to propagate without obstacles within the electrode porosity during their adsorption. These observations are consistent with NMR investigations on an EDLC in ref. [41], where an increase of the in-pore diffusion coefficient of tetrafluoroborate (BF_4^-) anions with the potential of the positive electrode was observed. In this potential range, the D2 band is upshifted up to approximately 1355 cm^{-1} (Fig. 8**c**), due to the stiffening of C-C bonds provoked by the progressive injection of holes, in good agreement with the results observed on anodically doped single-wall carbon nanotube electrodes with 1 mol L^{-1} $TEABF_4$ in acetonitrile electrolyte [44]. The rapid increase in electrode thickness found by ECD from 3.8 to 4.5 V *vs.* Li/Li^+ can then be related to the structural elongation of C-C bonds, facilitating anion adsorption as the potential increases relative to *PZC* [37]. This phenomenon induces defects in the material, explaining the significant increase in the I_{D1}/I_{G1} ratio in this potential range. This statement is in good agreement with the increase of I_{D1}/I_{G1} ratio, from 0.38 to 0.83,

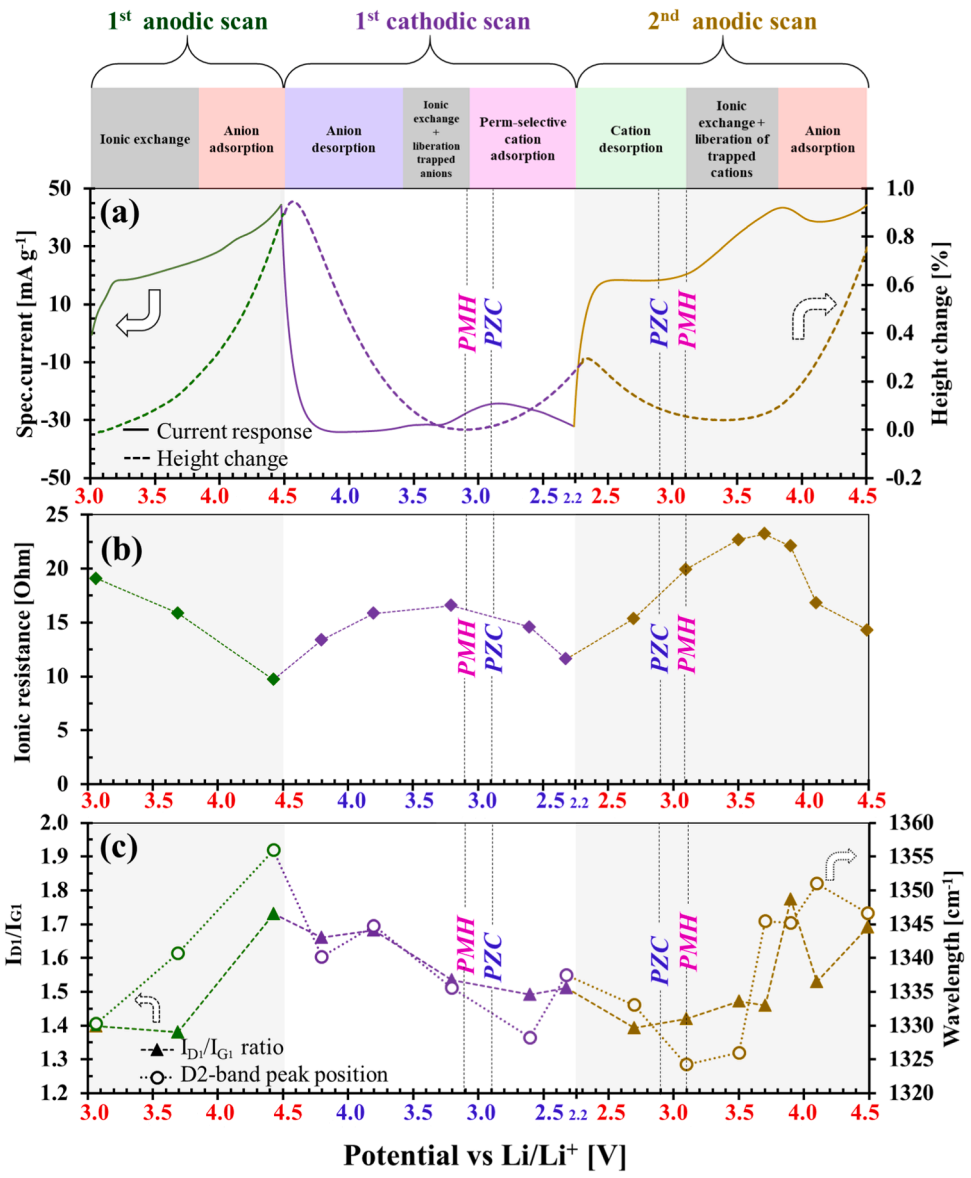

Fig. 8. (a) Specific current (solid line) and relative height change (dashed line) from *operando* electrochemical dilatometry; (b) ionic resistance from *in situ* PEIS; and (c) I_{D1}/I_{G1} peaks intensity ratio and D2 band position from *operando* Raman spectroscopy on an AC-based electrode in 1 mol L^{-1} $LiPF_6$/EC:DMC during scanning the potential at 0.25 mV s^{-1}, with 1st anodic scan from *OCP* to 4.5 V *vs.* Li/Li^+, followed by 1st cathodic scan to 2.2 V *vs.* Li/Li^+, and subsequent anodic scan to 4.5 V *vs.* Li/Li^+. *PZC* is the point of zero charge and *PMH* is the point of minimum height.

observed when an ionic liquid (1-hexyl-3-methylimidazolium bromide) is confined within the channel of multiwalled carbon nanotubes (MWCNTs) [47].

During the first cathodic scan (see Fig. 8, purple line), where the electrode potential decreases from 4.5 V *vs.* Li/Li^+ to approximately the *PZC*, R_{ionic} increases while the I_{D1}/I_{G1} ratio and Raman frequency of the D2 band decreases, all returning to nearly their initial values at *OCP*, demonstrating the reversibility of the phenomena observed during the 1st anodic scan. It is worth noting that the I_{D1}/I_{G1} ratio remains almost unchanged down to approximately 3.8 V *vs.* Li/Li^+, suggesting that the long-range electrostatic repulsions, caused by densely trapped anions into the electrode porosity during the first anodic scan, persist down to this potential, maintaining the level of disorder in the electrode [48]. The smooth evolution of the I_{D1}/I_{G1} ratio around 3.3 V *vs.* Li/Li^+ suggests the unchanged structural stress in the electrode in this potential region, likely due to the small number of trapped anions being liberated from the less accessible pores of the electrode.

When extending the first cathodic scan from the *PZC* to 2.2 V *vs.* Li/Li^+, R_{ionic} slightly decreases (see Fig. 8**b**), indicating the increase of in-pore ionic diffusion. Such behaviour does not match the results observed in ref. [41], where both cationic and anionic diffusion coefficients diminish with the potential of the negative electrode in an EDLC, due to perm-selective cation adsorption and the large size of tetraethylphosphonium cations (diameter = 0.72 nm). To explain this opposite trend in our case, it is important to consider that, according to MD simulations in the absence of polarization, partially solvated lithium cations (see Fig. 3**d**) may access the electrode porosity during the perm-selective cation adsorption. However, as the potential decreases relative to *PZC*, the lithium cations may lose their solvation shell, allowing their easy diffusion to less accessible pores, which could justify the slight decrease of R_{ionic}. The perm-selective adsorption of lithium cations, provoked by the electron injection in the electrode, does not significantly affect the structural features of the AC material (Fig. 8**c**). The I_{D1}/I_{G1} ratio stays almost unchanged, and the position of the D2 band is almost constant (note that the fluctuations of the D2-band peak position in this potential range are in the limit of measurement

accuracy), in agreement with the data presented in ref. [44] for such injection.

During the 2nd anodic scan from *PZC* to ca. 3.8 V *vs.* Li/Li$^+$, R_{ionic} increases up to values higher than in the 1st anodic scan (Fig. 8**b**, mustard line), coinciding with a peak in the current response and a constant electrode thickness (see Fig. 8**a**). This increase in R_{ionic} is likely due to trapped cations which hinder the mobility of anions into the porosity. Beyond this point, R_{ionic} decreases sharply as cations have been released, allowing easier anion diffusion. Between 3.8 and 4.5 V *vs.* Li/Li$^+$, the current returns to its capacitive response, the thickness continues to increase, and R_{ionic} decreases, revealing anion adsorption, as already observed in this potential range during the 1st anodic scan. The sudden increase of the I_{D1}/I_{G1} ratio, almost aligned with the maximum of the peak attributed to the desorption of trapped cations, can be explained by structural changes in the electrode due to quick swapping between trapped cations being liberated and anions trying to access the porosity.

4. Conclusion

This comprehensive study provides significant insights into in-pore ion population changes and reveals ion trapping phenomena in activated carbon (AC)-based electrode functioning as the positive electrode of a lithium-ion capacitor (LIC) during its charge/discharge cycles. Molecular dynamics (MD) simulations applied to the battery-type electrolyte (1 mol L^{-1} $LiPF_6$ in EC:DMC), both in its bulk state and within the porosity of a model carbon without an applied charge, show that ion-solvent interactions may play an important role in ion population changes during in-pore/ex-pore exchange processes.

Using various cutting-edge methods, including *operando* electrochemical dilatometry (ECD), *in situ* potentiostatic electrochemical impedance spectroscopy (PEIS), and *operando* Raman spectroscopy, the following potential-dependent phenomena and parameters were identified during cathodic (electron injection) and anodic (hole injection) polarization of the AC electrode:

i) During the initial anodic sweep above the point of zero charge (*PZC*, 2.9 V *vs.* Li/Li$^+$), ionic exchange followed by anion adsorption was observed, evidenced by an increase in electrode height and capacitive current. The significant decrease in ionic resistance during this phase, as observed through PEIS, indicates more rapid diffusion of PF_6^- anions, which are smaller than the partially solvated Li$^+$ cations previously occupying the pores before polarization.
ii) The subsequent cathodic polarization down to the point of minimum height (*PMH,* ca. 3.1 V *vs.* Li/Li$^+$) resulted in anion desorption, with a small amount of trapped anions being released near the *PMH*. This suggests that some anions became trapped in less accessible pores when the electrode was polarized above 3.8 V *vs.* Li/Li$^+$ during the anodic scan.
iii) Continued cathodic polarization below the *PMH* resulted in perm-selective adsorption of partially solvated Li$^+$ cations. This conclusion is supported by the much smaller capacitive current observed in this potential region compared to that recorded above the *PMH*, indicating limited access of the partially solvated Li$^+$ cations to the electrode porosity.
iv) During the subsequent anodic scan, these Li$^+$ ions are desorbed up to the *PMH*. Above the *PMH*, the same ionic exchange followed by anion adsorption occurred as in step (i). However, a peak at approximately 3.8 V *vs.* Li/Li$^+$ was observed in the CVs, attributed to the desorption of lithium cations trapped in the less accessible pores of the AC electrode.

The analysis of Raman spectra of the AC electrode during cycling has been instrumental in elucidating the induction of defects during the ionic exchange together with the liberation of trapped cations. This is evidenced by the increasing I_{D1}/I_{G1} ratio in these domains. The high polarization required to extract the trapped lithium ions from the AC porosity may explain the reduced lifespan of LICs, due to progressive degradation of the electrode material.

Overall, this study highlights the complex interplay between ionic exchange, anion adsorption/desorption, and cation trapping, which are critical for optimizing the performance and lifespan of LICs. Understanding and addressing properties of LICs related to ion desorption could help improve their performance. In particular, optimizing the porous texture of carbon materials to eliminate ion trapping should be a subject of further research.

CRediT authorship contribution statement

Andres Parejo-Tovar: Writing – original draft, Visualization, Software, Investigation, Formal analysis, Data curation. **Céline Merlet:** Writing – review & editing, Validation, Software. **Paula Ratajczak:** Validation, Project administration, Funding acquisition. **François Béguin:** Writing – review & editing, Visualization, Supervision, Resources, Project administration, Methodology, Funding acquisition, Conceptualization.

Declaration of competing interest

The authors declare that they have no known competing financial interests or personal relationships that could have appeared to influence the work reported in this paper.

Acknowledgments

This work was supported by the Foundation for Polish Science (research grants TEAM TECH/POIR.04.04.00–00–3D6F/16–00 and POWROTY/POIR.04.04.00–00–5EF5/18–00) and the Ministry of Science and Higher Education of Poland (Project 0911/SBAD/2401). The authors acknowledge Kuraray and Imerys for kindly providing samples of activated carbons and Super C65 carbon black, respectively.

Supplementary materials

Supplementary material associated with this article can be found, in the online version, at doi:10.1016/j.ensm.2024.103810.

References

[1] P. Ratajczak, M. Suss, F. Kaasik, F. Béguin, Carbon electrodes for capacitive technologies, Ener. *Stor. Mater.* 16 (2017) 126–145, https://doi.org/10.1016/j.ensm.2018.04.031.
[2] F. Béguin, V. Presser, A. Balducci, E. Frąckowiak, Carbons and electrolytes for advanced supercapacitors, Adv. Mater. 26 (2014) 2219–2251, https://doi.org/10.1002/adma.201304137.
[3] C. Zhong, Y. Deng, W. Hu, J. Qiao, L. Zhang, Z. Jiujun, A review of electrolyte materials and compositions for electrochemical supercapacitors, Chem. Soc. Rev. 44 (2015) 7484–7539, https://doi.org/10.1039/C5CS00303B.
[4] J. Krummacher, C. Schütter, S. Passerini, A. Balducci, Characterization of different conductive salts in acn-based electrolytes for electrochemical double-layer capacitors, ChemElectroChem. 4 (2017) 353–361, https://doi.org/10.1002/celc.201600534.
[5] Skeleton Technologies, "Skeleton," 2024. [Online]. Available: https://www.skeletontech.com/en/skelcap-supercapacitors. [Accessed 19 January 2024].
[6] A. Burke, J. Zhao, Past, present and future of electrochemical capacitors: technologies, performance, and applications, J. Ener. Storage 35 (2021) 102310–102333, https://doi.org/10.1016/j.est.2021.102310.
[7] J. Kowal, E. Avaroglu, F. Chamekh, A. Šenfelds, T. Thien, D. Wijaya, D.U. Sauer, Detailed analysis of the self-discharge of supercapacitors, J. Power Sources 196 (2011) 573–579, https://doi.org/10.1016/j.jpowsour.2009.12.028.
[8] A. Chojnacka, F. Béguin, Recent progress in the realization of metal-ion capacitors with alloying anodic hosts: a mini review, Electrochem. Commun. 139 (2022) 107305–107310, https://doi.org/10.1016/j.elecom.2022.107305.
[9] T. Aida, K. Yamada, M. Morita, An advanced hybrid electrochemical capacitor that uses a wide potential range at the positive electrode, Electrochem. Solid-State Lett. 9 (2006) A534–A536, https://doi.org/10.1149/1.2349495.
[10] JM energy & JSR micro, "ULTIMO 3300F, prismatic cell model," 2024. [Online]. Available: https://www.jsrmicro.be/emerging-technologies/lithium-ion-capacito

r/products/ultimo-lithium-ion-capacitor-prismatic-cell. [Accessed 19 January 2024].
[11] D. Cericola, R. Kötz, Hybridization of rechargeable batteries and electrochemical capacitors: Principles and limits, Electrochim. Acta. 72 (2012) 1–17, https://doi.org/10.1016/j.electacta.2012.03.151.
[12] B. Babu, P. Simon, A. Balducci, Fast charging materials for high power applications, *Adv.* Ener. *Mater.* 10 (2020) 2001128–2001161, https://doi.org/10.1002/aenm.202001128.
[13] J. Zheng, Energy density theory of lithium-ion capacitors, J. Electrochem. Soc. 168 (2021) 80503–80509, https://doi.org/10.1149/1945-7111/ac180f.
[14] M.D. Levi, N. Levy, S. Sigalov, G. Salitra, D. Aurbach, J. Maier, Electrochemical quartz crystal microbalance (EQCM) studies of ions and solvents insertion into highly porous activated carbons, J. Am. Chem. Soc 132 (2010) 13220–13222, https://doi.org/10.1021/ja104391g.
[15] M. Endo, T. Maeda, T. Takeda, Y.J. Kim, K.H.H. Koshiba, M.S. Dresselhaus, Capacitance and pore-size distribution in aqueous and nonaqueous electrolytes using various activated carbon electrodes, J. Electrochem. Soc. 148 (2001) A910–A914, https://doi.org/10.1149/1.1382589.
[16] J.-C. Soetens, C. Millot, B. Maigret, Molecular dynamics simulation of Li+BF4- in ethylene carbonate, propylene carbonate, and dimethyl carbonate solvents, J. Phys. Chem. A 102 (1998) 1055–1061, https://doi.org/10.1021/jp972457+.
[17] K. Xu, S. Ding, T.R. Jow, Toward reliable values of electrochemical stability limits for electrolytes, J. Electrochem. Soc. 146 (1999) 4172–4178, https://doi.org/10.1149/1.1392609.
[18] M. Thommes, K. Kaneko, A. Neimark, J. Olivier, F. Rodriguez-Reinoso, J. Rouquerol, K. Sing, Physisorption of gases, with special reference to the evaluation of surface area and pore size distribution (IUPAC Technical Report), Pure Appl. Chem. 87 (2015) 1051–1069, https://doi.org/10.1515/pac-2014-1117.
[19] J. Jagiello, NLDFT analysis by SAIEUS program, Micromeritics 05 (2021) [Online]. Available: https://saieus.com/ [Accessed 12 04 2023].
[20] M. Paalo, I. Tallo, T. Thomberg, A. Jänes, E. L, Enhanced power performance of highly mesoporous sol-gel tic derived carbons in ionic liquid and non-aqueous electrolyte based capacitors, J. Electrochem. Soc. 166 (2019) A2887–A2895, https://doi.org/10.1149/2.0721913jes.
[21] A. Ferrari, J. Robertson, Interpretation of raman spectra of disordered and amorphous carbon, Phys. Rev. B 61 (2000) 14095–14107, https://doi.org/10.1103/PhysRevB.61.14095.
[22] P.-L. Taberna, P. Simon, F. Béguin, E. Frąckowiak, Electrochemical techniques. Supercapacitors: materials, systems and applications, Wiley-VCH Verlag GmbH & Co. KGaA, 2013, pp. 111–130, https://doi.org/10.1002/9783527646661.ch3.
[23] Y. Shi, A mimetic porous carbon model by quench molecular dynamics simulation, J. Chem. Phys. 128 (2008), https://doi.org/10.1063/1.2943645, 234707_2-234707_11.
[24] D. Dubbelham, S. Calero, D. Ellis, R. Snurr, RASPA: molecular simulation software for adsorption and diffusion in flexible nanoporous materials, Mol. Simul. 42 (2016) 81–101, https://doi.org/10.1080/08927022.2015.1010082.
[25] L. Martinez, R. Andrade, E. Birgin, J. Martinez, PACKMOL: A package for building initial configurations for molecular dynamics simulations, J. Comput. Chem. 30 (2009) 2157–2164, https://doi.org/10.1002/jcc.21224.
[26] N. Schmid, A. Eichenberger, A. Choutko, A Riniker, M. Winger, A. Mark, W. van Gunsteren, Definition and testing of the GROMOS force-field versions 54A7 and 54B7, Eur. Biophys. J. 40 (2011) 843–856, https://doi.org/10.1007/s00249-011-0700-9.
[27] A. Thompson, M. Aktulga, B.D.R Berger, M. Brown, P. Crozier, P. Veld, A. Kohlmeyer, S. Moore, T. Nguyen, R. Shan, M. Stevens, J. Tranchida, C. Trott, S. Plimpton, LAMMPS - a flexible simulation tool for particle-based materials modeling at the atomic, meso, and continuum scales, Comput. Phys. Commun. 271 (2022) 108171–108204, https://doi.org/10.1016/j.cpc.2021.108171.
[28] A. Stukowski, Visualization and analysis of atomistic simulation data with OVITO–the Open Visualization Tool, Model. Simul. Mat. Sci. Eng. 18 (2010) 15012–15018, https://doi.org/10.1088/0965-0393/18/1/015012.
[29] S. Gharouel, F. Béguin, Revisiting the performance of electrical double-layer capacitors implementing a sodium perchlorate water-in-salt electrolyte, Electrochim. Acta 450 (2023) 142212–142221, https://doi.org/10.1016/j.electacta.2023.142212.
[30] M. Ong, O. Verners, E. Draeger, A. van Diun, V. Lordi, J. Pask, Lithium ion solvation and diffusion in bulk organic electrolytes from first-principles and classical reactive molecular dynamics, J. Phys. Chem. B 119 (2015) 1535–1545, https://doi.org/10.1021/jp508184f.
[31] T. Kartha, B. Mallik, Revisiting LiClO4 as an electrolyte for Li-ion battery: effect of aggregation behavior on ion-pairing dynamics and conductance, J. Mol. Liq 302 (2020) 112536–112545, https://doi.org/10.1016/j.molliq.2020.112536.
[32] J.M. Griffin, A.C. Forse, W.-Y. Tsai, P.-L. Taberna, P. Simon, C.P. Grey, In situ NMR and electrochemical quartz crystalmicrobalance techniques reveal the structure of the electrical double layer in supercapacitors, Nat. Mater 14 (2015) 812–819, https://doi.org/10.1038/nmat4318.
[33] P. Galek, P. Bujewska, S. Donne, M. J, New insight into ion dynamics in nanoporous carbon materials: an application of the step potential electrochemical spectroscopy (SPECS) technique and electrochemical dilatometry, Electrochim. Acta 377 (2021) 138115–138121, https://doi.org/10.1016/j.electacta.2021.138115.
[34] H. Yin, H. Shao, B. Daffos, P.-L. Taberna, P. Simon, The effects of local graphitization on the charging mechanisms of microporous carbon supercapacitor electrodes, Electrochem. Commun. 137 (2022) 107258–107262, https://doi.org/10.1016/j.elecom.2022.107258.
[35] M. Hahn, M. Baertschi, O. Barbieri, J.-C. Sauter, R. Kötz, R. Gallay, Interfacial capacitance and electronic conductance of activated carbon double-layer electrodes, Electrochem. Solid-State Lett. 7 (2004) A33–A36, https://doi.org/10.1149/1.1635671.
[36] W.-Y. Tsai, P.-L. Taberna, P. Simon, Electrochemical quartz crystal microbalance (EQCM) study of ion dynamics in nanoporous carbons, J. Am. Chem. Soc. 136 (2014) 8722–8728, https://doi.org/10.1021/ja503449w.
[37] M.M. Hantel, D. Weingarth, R. Kötz, Parameters determining dimensional changes of porous carbons during capacitive charging, Carbon. N. Y. 69 (2014) 275–286, https://doi.org/10.1016/j.carbon.2013.12.026.
[38] D. Aurbach, M. Levi, G. Salitra, N. Levy, E. Pollak, J. Muthu, Cation trapping in highly porous carbon electrodes for edlc cells, J. Electrochem. Soc. 155 (2008) A745–A753, https://doi.org/10.1149/1.2957911.
[39] J. Black, G.F.P. Feng, P. Hillesheim, S. Dai, Y. Gogotsi, P. Cummings, S. Kalinin, N. Balke, Strain-based in situ study of anion and cation insertion into porous carbon electrodes with different pore sizes, *Adv.* Ener. *Mater.* 4 (2014) 1300683–1300690, https://doi.org/10.1002/aenm.201300683.
[40] Q. Gao, W. Tsai, N. Balke, In situ and operando force-based atomic force microscopy for probing local functionality in energy storage materials, Electrochem. Sci. Adv. 2 (2022) 2100038–2100064, https://doi.org/10.1002/elsa.202100038.
[41] A. Forse, J.M. Griffin, C. Merlet, J. Carretero-Gonzalez, A.-R. Raji, N.M. Trease, C. Grey, Direct observation of ion dynamics in supercapacitor electrodes using in situ diffusion NMR spectroscopy, *Nat.* Ener. 2 (2017) 16216–16222, https://doi.org/10.1038/nenergy.2016.216.
[42] F. Bonhomme, C. Lassegues, L. Servant, Raman spectroelectrochemistry of a carbon supercapacitor, J. Electrochem. Soc. 148 (2001) E450–E458, https://doi.org/10.1149/1.1409546.
[43] L. Hardwick, P. Ruch, M. Hahn, W. Scheifele, R. Kötz, P. Novák, In situ Raman spectroscopy of insertion electrodes for lithium-ion batteries and supercapacitors: first cycle effects, J. Phys. Chem. Solids 69 (2008) 1232–1237, https://doi.org/10.1016/j.jpcs.2007.10.017.
[44] P. Ruch, L. Hardwick, M. Hahn, A. Foelske, R. Kötz, A. Wokaun, Electrochemical doping of single-walled carbon nanotubes in double-layer capacitors studied by in situ Raman spectroscopy, Carbon N. Y. 47 (2009) 38–52, https://doi.org/10.1016/j.carbon.2008.08.023.
[45] R. Venâncio, R. Vicentini, L. Costa, R. Teófilo, L. Silva, H. Zanin, In-situ electrochemical and operando Raman techniques to investigate the effect of porosity in different carbon electrodes in organic electrolyte supercapacitors, J. Ener. Storage 50 (2022) 104219–104230, https://doi.org/10.1016/j.est.2022.104219.
[46] A. Coccato, J. Jehlicka, L. Moens, P. Vandenabeele, Raman spectroscopy for the investigation of carbon-based black pigments, J. Raman Spectrosc. 46 (2015) 1003–1015, https://doi.org/10.1002/jrs.4715.
[47] F. Jiang, C. Li, H. Fu, C. Wang, X. Guo, Z. Jiang, G. Wu, S. Chen, Temperature-induced molecular rearrangement of an ionic liquid confined in nanospaces: an in situ x-ray absorption fine structure study, J. Phys. Chem. C 119 (2015) 22724–22731, https://doi.org/10.1021/acs.jpcc.5b07325.
[48] K. Kiyohara, T. Sugino, S. Asaka, Electrolytes in porous electrodes: effects of the pore size and the dielectric constant of the medium, J. Chem. Phys. 132 (2010) 144705–144716, https://doi.org/10.1063/1.3376611.